University of Zagreb Faculty of Mechanical Engineering and Naval Architecture

journal homepage: www.brodogradnja.fsb.hr

Brodogradnja

An International Journal of Naval Architecture and Ocean Engineering for Research and Development

An investigation of ice resistance and turning ability for polar ships in brash ice areas using CFD-DEM integrated approach

Jinlong Zhang[1], Jianing Zhang[1,], Zitian Liao[1], Lei Zhang[1], Kefu Qi[1], Haihua Zhang[2], Feng Diao[2]*

[1] *School of Naval Architecture and Ocean Engineering, Dalian Maritime University, Dalian 116026, PR China*
[2] *Taihu Laboratory of Deepsea Technological Science Lian Yun Gang Center, Lianyungang 222000, China*

ARTICLE INFO

Keywords:
Ice resistance
Turning ability
CFD-DEM
Ice geometry
Young's modulus
Rudder angle

ABSTRACT

To elucidate the operational performance characteristics of polar ships navigating through brash ice areas, this study systematically investigates ship ice resistance and turning ability through an integrated approach combining CFD-DEM numerical simulations and model tests. The DFBI plane motion was employed to simulate the interaction between a polar ship and brash ice, the maximum deviation of ice resistance among the numerical simulation results, the FSICR formula, and the model test data is 15.87 %. Validating the reliability of the numerical model and methodology. The body force method and overset grid technology were employed to establish a turning ability simulation model, triangular, circular and square brash ice region environments are constructed. Analysis of key influencing factors reveals that, under constant brash ice concentration conditions, triangular brash ice shapes significantly increase both ice resistance and turning diameter. High sea ice Young's modulus increases ice resistance and turning diameter, thus diminishes turning ability. The deceleration effect of polar ships under small rudder angle conditions is weaker than that under large rudder angle conditions, while the corresponding magnitudes of ice resistance and heave motion responses are higher. This research provides a methodological reference for the investigation of ship's turning ability.

1. Introduction

Due to global climate warming and the consequent retreat of Arctic sea ice, polar shipping routes have become increasingly accessible during the navigable season. For polar transport ships, safe and efficient operation in ice-covered waters depends not only on resistance performance but also on the ability to maintain heading, execute turning maneuvers, and avoid local ice accumulation during navigation. Compared with open-water conditions, ship motion in ice-covered waters is affected by repeated ship–ice collisions, asymmetric longitudinal and transverse ice loads, local flow-field variations, and speed loss, all of which may significantly degrade turning performance. In practical operations, ships more frequently encounter floating ice, pack ice, and brash-ice channels rather than ideal continuous level ice. Therefore, investigating the turning

* Corresponding author.
E-mail address: zhangjianing@dlmu.edu.cn

https://doi.org/10.21278/brod78101
Received 29 January 2026; Received in revised form 09 June 2026; Accepted 02 September 2026
Available online 23 September 2026
ISSN 0007-215X; eISSN 1845-5859

ability of polar ships in brash-ice regions is of direct engineering significance for navigation safety, route planning, and ship design.

Recent numerical studies on ship–ice interaction in brash-ice environments have increasingly relied on coupled CFD-DEM frameworks, because they can simultaneously account for fluid effects and discrete ice collisions. Huang et al. [1] developed a combined CFD&DEM approach for ship resistance in floating ice floes and highlighted the importance of wave effects and random natural floe fields in high-fidelity prediction. Luo et al. [2] applied a CFD-DEM method to an ice-strengthened bulk carrier in a brash ice channel and demonstrated that including ship–water interaction improves the prediction of resistance. Xie et al. [3] further extended CFD-DEM to self-propulsion simulations in brash ice channels using the body force model, showing that the method provides acceptable accuracy with substantially improved computational efficiency. More recently, Zou et al. [4] proposed a simplified CFD-DEM framework with realistic polyhedral brash-ice modelling and investigated the longitudinal and lateral distributions of ice force on a ship.

Research on the maneuverability of ships operating in ice-covered water remains relatively limited. Under complex ice conditions, the accuracy of the empirical formula method remains uncertain, and it is incapable of addressing ship maneuverability issues. Some scholars have developed ice-breaking maneuvering models by virtue of algorithms, whereas the CFD method is primarily applied to the numerical calculation of ship ice resistance in straight-line navigation. Ice-tank model tests are often employed to obtain ice loads and to reproduce level-ice breaking scenarios. More recently, data-driven and machine learning techniques have been applied to experimental values to develop predictive models for ice resistance. From the viewpoint of maneuvering prediction, Yasukawa and Yoshimura [5] introduced the MMG method, which provides a widely accepted framework for decomposing hull, propeller, and rudder forces in ship maneuvering simulation. Kim et al. [6] experimentally and numerically investigated ship–ice interaction in pack ice by combining free-running model tests with a DEM-based numerical model and showed that turning behavior in ice differs markedly from that in open water. Zhou et al. [7] further developed a three-degree-of-freedom numerical model for ships advancing and turning in level ice, and emphasized that, during turning, transverse force and yaw moment are as important as longitudinal resistance. More recently, Yang et al. [8] compared two turning modes of a ship in brash ice based on the non-smooth discrete element method and reported that star maneuver, although more complex, may effectively reduce the turning area required under high or uncertain ice conditions. Wang et al. [9] developed a coupled NDEM–MMG framework for non-icebreaking ships in floating ice and systematically analyzed the effects of ice concentration, floe size, and rudder angle on turning-circle and zig-zag performance. In earlier years, Lau et al. [10] developed DECICE code to analyze the maneuvering performance of the icebreaker Terry Fox in level ice, validating results through PMM towing tests and conducting additional analysis on the effects of ship motions on resistance and moment. Zhan et al. [11] adopted the Ship Maneuvering Laboratory code to calculate ship hydrodynamics, and while employing the DECICE program to compute ice loads and ship motions, they predicted the turning and Zig-zag maneuvering under both ice-covered and open water environments.

From the perspective of broader numerical modelling, the coupled CFD-DEM approach has shown clear advantages in resolving both discrete ice collisions and local hydrodynamic effects, and has been applied to floating ice, brash ice, and level-ice scenarios. This method not only enables quantitative evaluation of ice loads during impact events but also provides high-fidelity resolution of the flow fields around the propeller and rudder. Consequently, it proves effective for simulations across various ice conditions, including floating ice, brash ice, and level ice [12-15].

Meanwhile, FEM-, SPH-, and hybrid-method-based studies have also been widely used to investigate ice loads, hull stress responses, and ice-failure processes under different ice conditions. Li et al. [16] integrated probabilistic statistics with FEM simulations, validating the effectiveness of the proposed approach against experimental results. Their study further investigated the variation patterns of ice loads acting on the bow, midship, and stern of the Xue Long icebreaker during straight-line navigation and turning maneuvers. The FEM method can be applied to predict ice loads and stress on ships. Later, the ship-ice collision process in brash ice region was simulated, with calculated ice load results under different ship speeds and ice concentrations validated against experimental data [17-19]. Liu et al. [20] employed a PD-FEM coupled approach to simulate the ship speed and ice thickness on ice loads, The numerical results showed agreement with Lindqvist empirical formula.

Research on the FEM-SPH method, focusing on the interaction between conical structures, icebreakers, and level ice, numerically simulated the accumulation and movement phenomena of brash ice particles and revealed the effects of cone angles and heading angles on ice loads [21, 22]. Xu et al. [23] employed a FEM-SPH coupled method to investigate ship-ice interactions, the results revealed a positive correlation between ice resistance and ship speed and further demonstrated that the load oscillation amplitudes at the bow were markedly lower than those at the stern. An improved SPH_SFDI method was proposed, and it was demonstrated that this approach can significantly enhance the accuracy of simulating bending and compression failures of ice [24, 25].

More direct investigations of ship maneuvering performance in ice-covered waters have gradually emerged in recent years. Comparative analysis of numerical simulations and full-scale trials revealed substantial ice load generation at the aft shoulder region of the icebreaker Tor Viking II during turning maneuvers, with ice load characteristics influenced by hull shape, operational modes, and icebreaking patterns. The inward heel of polar ships enhances turning ability, reducing the turning circle diameter by 30% during astern navigation [26-28]. In addition, numerical predictions of ice loads during ship-level ice collisions and ship maneuvering parameters in level ice were validated against experimental data, confirming the accuracy of the numerical methods [29, 30]. LS-DYNA was used to determine ice loads and lateral forces on the Xue Long, analyzing their dependence on drift angle and turning radius, EDEM software further quantified the effects of turning radius, drift angle, sway, and yaw periods on ice loads [31, 32]. Yang et al. [33] used a combined NDEM-MMG to study the Xue Long ship's maneuvering, examining the effects of brash ice size and ship speed on turning and Zig-zag maneuvers, as well as identifying ice load trends. Zhang et al. [34] used the CFD-DEM and MMG models to predict polar ship maneuverability in open water and brash ice, focusing on ice thickness and shape effects, and providing validated turning trajectories and ice resistance predictions.

The limitation of polar ship maneuverability lies in how to achieve high-precision monitoring of ship turning trajectories, accurate prediction of ice-water resistance, and precise capture of the flow field during polar ship maneuvering. Meanwhile, a notable commonality in existing research is the predominant focus on numerical and experimental investigations of ice resistance in straight-line navigation, self-propulsion performance, and local-force force distribution, while systematic discussions on ship maneuverability in diverse polar ice environments remain limited. Critical aspects such as the influence of ice parameters on maneuvering performance, the effects of different ice shapes and sizes, and the role of rudder angles on ship response have received insufficient attention. These parameters collectively govern multiple facets of ship-ice interactions, including directional variations in ice resistance, maneuvering trajectories, resultant ship velocity, and rudder force in different directions.

In this study, a coupled CFD-DEM method is used to simulate the turning maneuvers of a polar ship navigating through brash ice. A body-force virtual disk method and overset grid technique are used to conduct sensitivity analyses of ice resistance and maneuverability parameters. This method not only balances computational efficiency and accuracy but also avoids the complex meshing issues associated with propeller blade geometry by using the body force method. Furthermore, the CFD-DEM framework can provide descriptions of the local flow characteristics and brash ice motion around the hull during maneuvering processes. The results provide predictions of ice resistance and maneuvering trajectories in brash ice conditions, offering theoretical insights to support safe ship operations, ship design, and navigational strategies in the polar region.

2. Numerical method

2.1 RANS equations

In the current investigation, the numerical simulation of viscous flow is formulated Based on the Reynolds-averaged Navier-Stokes (RANS) equations, the governing equations consist of the continuity equation representing mass conservation and the momentum conservation equation, expressed as follows:

$$\nabla \cdot \overline{\boldsymbol{u}} = 0 \tag{1}$$

$$\frac{\partial\left(\rho_f \overline{\boldsymbol{u}}\right)}{\partial t} + \nabla \cdot \left(\rho_f \overline{\boldsymbol{u}\boldsymbol{u}}\right) = -\nabla \overline{p} + \nabla \cdot \left(\overline{\boldsymbol{\tau}} - \rho_f \overline{\boldsymbol{u}'\boldsymbol{u}'}\right) + \rho_f \boldsymbol{g} \tag{2}$$

where $\overline{\boldsymbol{u}}$ and $\overline{p}$ represent the time-averaged velocity and pressure of the fluid, respectively; $\overline{\boldsymbol{\tau}}$ denotes the viscous stress tensor; $\rho_f \overline{\boldsymbol{u}'\boldsymbol{u}'}$ is the Reynolds stress term; and ρ_f and $\boldsymbol{g}$ denote the fluid density and gravitational acceleration, respectively.

2.2 Body-force method

When using a real propeller for numerical simulation, because the real rotation of the propeller takes a long time, in this paper, the body force method is used instead of the propeller to generate thrust to make the ship carry out self-propulsion turning and maneuvering motion. The body force method (BFM) is used to model the equivalent thrust and torque of the propeller. Compared with the simulation of real propeller geometry, this method can reduce the number of grids and improve computational efficiency. It does not need to obtain the detailed flow field around the propeller but only needs the correct propulsion specification. In this method, the body force F_b is uniformly distributed on the cylindrical virtual disk, and the body force changes in the radial direction. The radial distribution of the component force follows Goldstein's optimal distribution, and the calculation formula is as follows:

$$f_{bx} = A_x r^* \sqrt{1 - r^*} \tag{3}$$

$$f_{b\theta} = A_\theta \cdot \frac{r^* \sqrt{1 - r^*}}{r^* (1 - r_h') + r_h'} \tag{4}$$

where:

$$A_\theta = \frac{105}{8} \frac{Q}{\pi \Delta R_P \left(3R_H + 4R_P\right)\left(R_P - R_H\right)} \tag{5}$$

$$A_x = \frac{105}{8} \frac{T}{\pi \Delta \left(3R_H + 4R_P\right)\left(R_P - R_H\right)} \tag{6}$$

$$r^* = \frac{r' - r_h'}{1 - r_h'} \tag{7}$$

In these formulas, f_{bx} and $f_{b\theta}$ represent the distribution of axial force and circumferential momentum source, respectively, r represents the radical coordinate, R_H represents the hub radius, R_P represents the propeller radius. Δ represents the thickness of the virtual propeller, and A_x and A_θ are both constant. In addition, $r_h' = R_H / R_P$, $r' = r / R_P$, r' and r_h' are normalized expressions of r and R_H, r^* represents the radial distance from the paddle hub. Q and T represent torque and thrust respectively.

2.3 DEM contact model and particle injector model

The discrete element method, which was first proposed by Cundall and Stack [35], is used to model the brash ice particles and simulate the ship's turning and maneuvering in the brash ice region. There are three kinds of contact models available in DEM calculation software, namely the Hertz-Mindlin contact model, the Linear Spring contact model, and the Walton Braun contact model [36]. Considering the computational efficiency, the linear spring contact model is selected in this paper.

The repulsive force from the spring drives the discrete elements, and the damper models the damping effect, enabling the simulation of non-perfectly elastic collisions. At the contact point, the force model is constructed as a pair of oscillators consisting of a spring-damper, as shown in the discrete element contact model in Figure 1.

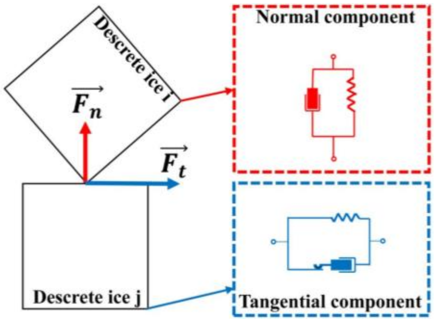

Fig. 1 Discrete element contact force model

The forces between two spheres, A and B, are:

$$F_{contact} = F_n n + F_t t \tag{8}$$

The normal force is:

$$F_n = -K_n d_n - N_n v_n \tag{9}$$

The tangential force is:

$$F_t = \begin{cases} -K_t d_t - N_t v_t & , \text{ if } |K_t d_t| \le |K_n d_n| C_{fs} \\ \dfrac{|K_n d_n| C_{fs} d_t}{|d_t|} & , \text{ if } |K_t d_t| > |K_n d_n| C_{fs} \end{cases} \tag{10}$$

where F_n and F_t are the magnitudes of the normal and tangential components, respectively. K_n is the normal spring stiffness, K_t is the tangential spring stiffness, N_n is the normal damping, N_t is the tangential damping, d_n is the overlap in the normal direction, d_t is the overlap in the tangential direction, v_n is a normal component of relative sphere surface velocity at the contact point, v_t is the tangential component of relative sphere surface velocity at the contact point, C_{fs} represents the friction coefficient.

In this study, brash ice particles are introduced onto the water surface via a component surface mesh method. Prior to the ship's turning maneuver, brash ice particles are injected into the water surface using the particle injector until the preset ice concentration is achieved. The function of the particle injector is to emit the brash ice particles simulated by the Lagrangian term into the continuous fluid to participate in numerical calculation, and it is also an important setting for the construction of different brash ice environments in this paper, and the concentration of the brash ice is controlled by adjusting the injector's flow rate.

2.4 Equation of motion for particle model

In the Discrete Element Method solution, each element satisfies its corresponding equation of motion. The overall kinematic state of the discrete medium is obtained through time-step iteration of individual element motion equations. Particle motion comprises translational and rotational components. For a simple particle element, the governing equations within a single time step are given by:

$$m_i \frac{dv_i}{dt} = \sum_j \mathbf{F}_{c,ij} + \sum_k \mathbf{F}_{ir,ik} + \mathbf{F}_{pf,i} + \mathbf{F}_{g,i} \tag{11}$$

$$I_i \frac{dw_i}{dt} = \sum \left(M_{t,ij} + M_{r,ij} \right) \tag{12}$$

where m_i is the mass of particle i, v_i is the velocity vector of the particle centroid, $F_{c,ij}$ represents the contact force between particles, $F_{ir,ik}$ denotes the non-contact force between particles. $F_{pf,i}$ is the particle-fluid interaction force, and $F_{g,i}$ is the gravitational force acting on the particle. I_i is the moment of inertia, w_i is the angular velocity of particle, $M_{t,ij}$ is the sliding friction torque, and $M_{r,ij}$ is the rolling friction torque.

2.5 The establishment of the coordinate system for polar ship

A multi-degree-of-freedom motion model of the ship in open water and brash ice areas is established, numerical simulations are employed to obtain the ship's turning maneuvering trajectories, the propeller thrust and rudder steering torque acting on the ship in brash ice areas are calculated. This study primarily investigates the impact of brash ice on ship maneuverability, with the environmental disturbance force being the ice resistance.

Before combining the body-force virtual disk method with the overset grid technique for maneuverability prediction, it is first necessary to establish the ship motion coordinate system. As shown in Figure 2, three coordinate systems are employed in the present study. The origin of the earth-fixed global coordinate system is denoted by O_0-$x_0y_0z_0$, the origin O_0 coincides with the polar ship's center of gravity G at t=0. A body-fixed coordinate system O-xyz is attached to the polar ship model, with its origin at G, this corresponds to the secondary coordinate system. In addition, a tertiary coordinate system, O_R-$x_Ry_Rz_R$, was established to define and control the rudder rotation angle. In the ship-fixed system, the longitudinal and lateral velocity components are denoted by u and v, respectively, and the resultant speed is $V=(u^2+v^2)^{1/2}$. G represents the center of gravity of the polar ship. The heading angle φ is defined as the counterclockwise angle from the O_0x_0 axis to the Gx axis, and the drift angle is defined as $\beta = \arctan(-v/u)$.

Coordinate transformation is then performed using Equation (13).

$$\begin{cases} x_0 = x_{0G} + x\cos\varphi - y\sin\varphi \\ y_0 = y_{0G} + x\sin\varphi + y\cos\varphi \\ z_0 = z \end{cases} \tag{13}$$

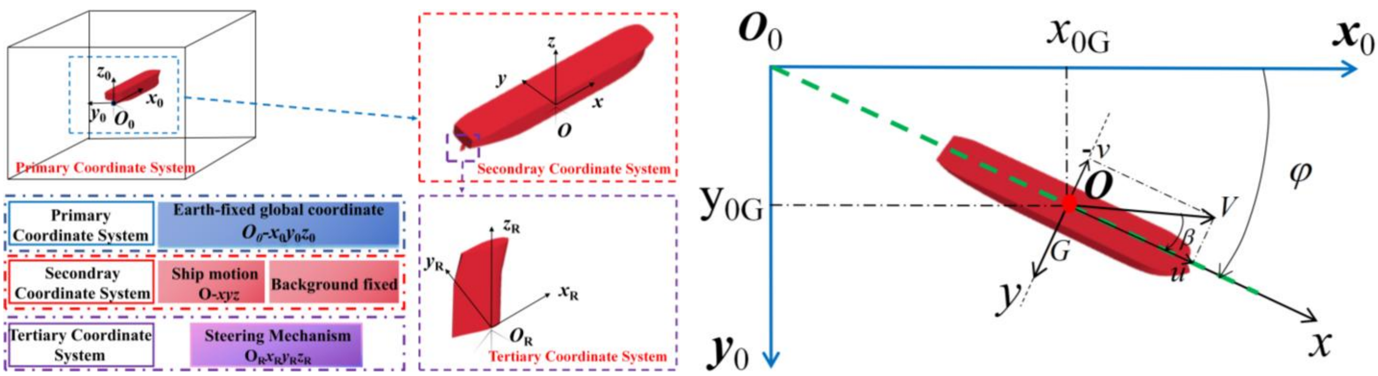

(a) Calculated coordinate system (b) Fixed coordinate system and hull coordinate system

Fig. 2 Multistage coordinate system

3. Ship-ice collision model test

This section mainly validates the proposed ship-ice collision model and brash ice resistance prediction method by comparing the numerical simulation results with existing HSVA ice tank experimental data. The primary objective is to evaluate the rationality and reliability of the numerical model in terms of ship-ice contact and brash ice resistance.

3.1 HSVA ice tank model test

The research object of this paper is a polar transport ship with an invisible bulbous bow, and towed propulsion tests were carried out in the HSVA ice tank [37]. The main dimension data of the model ship and the full-scale ship are shown in Table 1. Figure 3 shows the geometry of the ship model.

Table 1 The main dimensions of the model ship and the full-scale ship by HSVA

Principal hull data	Abbreviation	Unit	Full- scale	Model-scale
Scaling factor	λ	—	1	29.508
Length between perpendiculars	L_{pp}	m	223.400	7.571
Length at waterline	L_{UIWL}	m	226.800	7.686
Breadth moulded at DWL	B_{DWL}	m	32.260	1.093
Ice Waterline	T	m	13.3	0.451
Volume of displacement	$DISV$	m^3	82784	3.222
Wetted surface area	S	m^2	12021	13.806

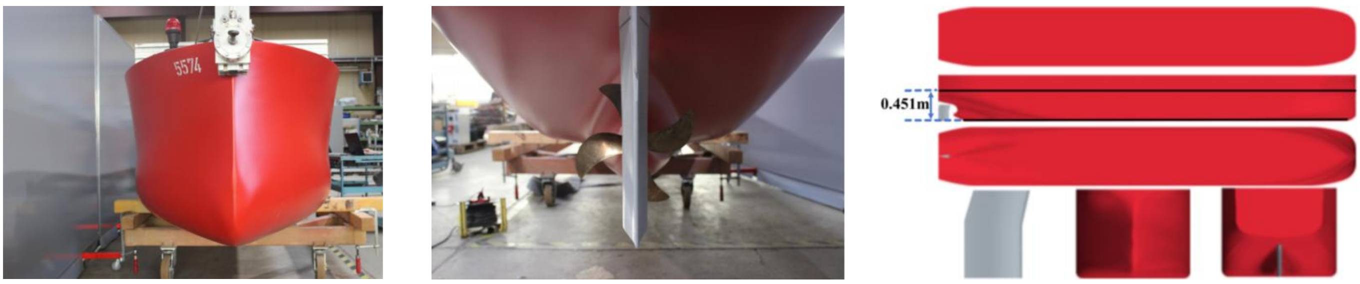

(a) Fore body of model-bow view (b) Aft body ship model back view (c) Ship–rudder numerical model

Fig. 3 Bow and stern view of the ship model

Hamburg's current level ice model is frozen in a natural way from a 0.7 % sodium chloride solution, the ice surface is exposed to cold air, the air temperature in the ice tank rises after the level ice thickness reaches a predetermined thickness, and when the air temperature is close to -2°C, an ice channel with straight edges is cut into the ice sheet. This is done by means of two ice knives being pushed by the auxiliary carriage. Thereafter, the ice stripe between the two cuts is manually broken up into relatively small ice pieces using special ice chisels. And carefully stir to achieve the most realistic appearance of the brash ice channel. Figure 4 shows the preparation process of the brash ice channel.

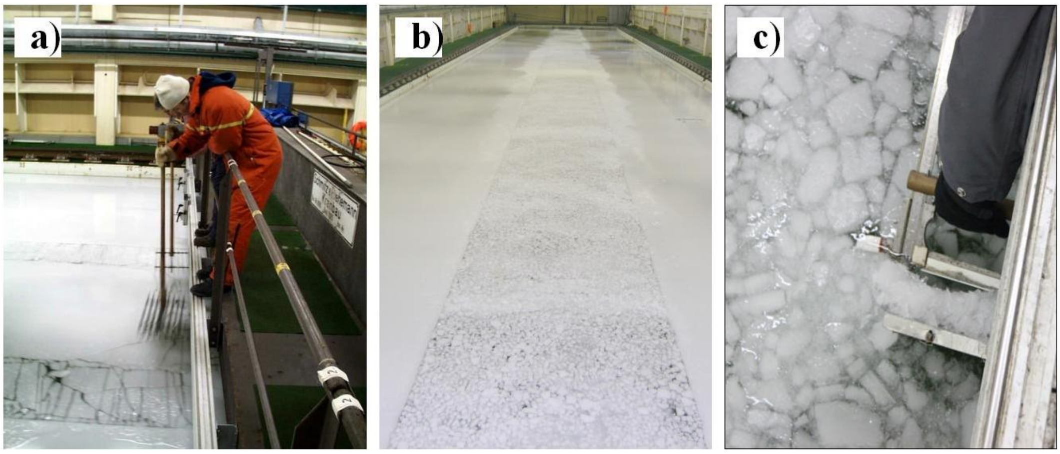

Fig. 4 Brash ice channel in HSVA experiments. (a) Preparation of brash ice; (b) Brash ice channel; (c) Reading the ice thickness

3.2 Comparison of numerical methods and experiments for ice resistance in brash ice channel

In the HSVA ice tank test, the model ship was towed continuously through the entire brash ice channel, and the speed of the carriage was set to 0.474 m/s. According to the ice class rules, the target friction coefficient was 0.1. The sea ice exhibits a Young's modulus of 290 MPa and a Poisson's ratio of 0.3. A spring stiffness of 1000 N/m was assigned in the model, the target brash ice thickness was 49.207 mm, the shape of the ejected brash ice particles is set as square, with a side length of 67.778 mm, the injected brash ice particles were uniformly distributed and neatly spread across the water surface, and the ice concentration was 65.22 %. Table 2 presents the relevant parameters of the brash ice used in the numerical simulations.

Table 2 Brash ice parameters in numerical simulation

Ice parameters	Target Friction Coefficient	Young's Modulus (Mpa)	Possion's Ratio	Spring Stiffness (N/m)	Ice Concentration (%)
Value	0.1	290	0.3	1000	65.22

In the numerical simulation, the overlapping grid method is used to set a plane motion mechanism in the DFBI so that the ship moves forward at a constant speed. When the ship collides with the brash ice, the velocity field of the brash ice particles in the water surface at different moments is shown in Figure 5. During the transition process from the initial entry of the ship into the brash ice channel to its full immersion within the channel, the brash-ice velocity field exhibited pronounced spatial non-uniformity. The yellow area shows that the brash ice particles at the bow of the ship show obvious acceleration after colliding with the ship, while the brash ice particles on both sides of the ship in the narrow channel have a smaller speed.

Most scholars adopt the relative motion method, which keeps the ship model stationary while brash ice collides with the ship model under the action of flow [38-41]. However, this section more realistically simulates the process of a ship model navigating through brash ice channel at a constant speed. Employing the Discrete Element Method, our team has numerically validated the ship-ice interaction model and brash ice resistance prediction capability for a polar transport ship, the numerical predictions for ice resistance and propulsion performance agree well with experimental data. The towed propulsion model tests, the numerical results of ice resistance, and the FSICR empirical formula are shown in Figure 6.

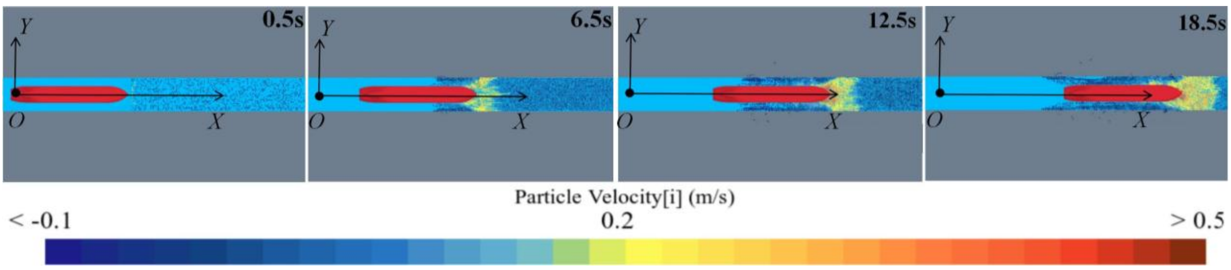

Fig. 5 The velocity field of the brash ice particles at the water surface

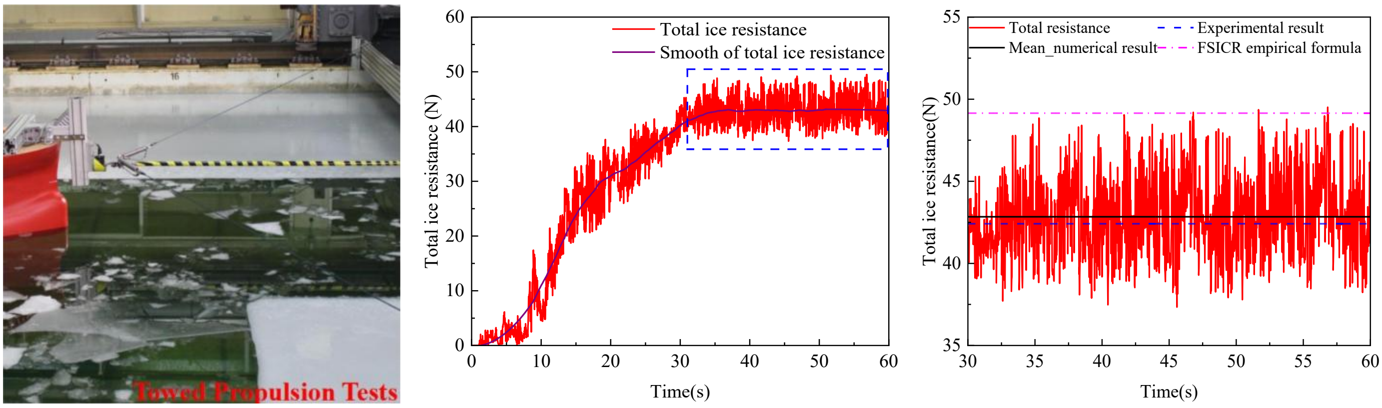

Fig. 6 Towed propulsion tests in HSVA and time-history curves of the total ice resistance

Table 3 Comparison of model test, FSICR empirical formula and CFD simulation results.

Ice thickness (mm)	Total Ice resistance (N)		
49.207	Model test result (N)	Average values of the numerical simulations (N)	FSICR empirical formula (N)
	42.414	42.836	49.147
Relative error (%)	baseline	0.99	15.87

From the flow field diagram, it is observed that the brash ice at the ship bow shows significant acceleration after the collision, while obvious ice accumulation occurs along both sides of the polar ship, where the ice particle velocity is noticeably lower. This momentum loss is responsible for the formation of the pressure peak at the bow and constitutes the primary source of the rapid increase in ice resistance during the initial stage. The mean numerical ice resistance, the experimental measurement, and the result predicted by the FSICR empirical formula are 42.836, 42.414, and 49.147 N, respectively. Table 3 provides the averages and errors obtained from the numerical simulations; the errors of numerical results, empirical formula results, and experimental results of ice resistance are less than 15.87 %. The reliability of the numerical model and the methodology’s accuracy were both verified.

4. Model Setup and Numerical Preprocessing

4.1 Propeller virtual disk setup and steering

The motion of the model ship is self-propulsion. First, the speed of the target ship is accelerated from 0 m/s to the specified speed. After reaching a steady velocity, the right steering operation was carried out, and the rudder was stopped after it turned to the specified rudder angle at a constant speed. In the test, the fluid domain is set to static, meaning that forces from waves and wind are neglected, and the ship is assumed to be sailing on deep, calm water. According to IMO’s ship maneuverability standard, the test speed must not be less than 90 % of the ship speed at the maximum output power of the corresponding 85% main engine power, and the model ship’s speed is set to 1.22 m/s.

In numerical calculations, the body force method is used to generate thrust instead of a propeller to make the model ship carry out self-propulsion turning motion. The body force method is used to model the equivalent thrust and torque of propeller. Compared with the real propeller geometric model, this method can reduce the number of grids and calculation cost, as it does not require resolution of the detailed flow field around the propeller blades but only an accurate representation of the propulsion forces. For numerical setup, the inner and outer diameters of the virtual disk are set to 0.037 and 0.244 m, respectively, and the virtual disk thickness is 0.1 m. The virtual disk settings in the simulation are shown in Figure 7. Table 4 presents the inner and outer diameters of the virtual disk for the polar ship, as well as the ship's center of mass coordinates, total model ship mass, and the moment of inertia parameters.

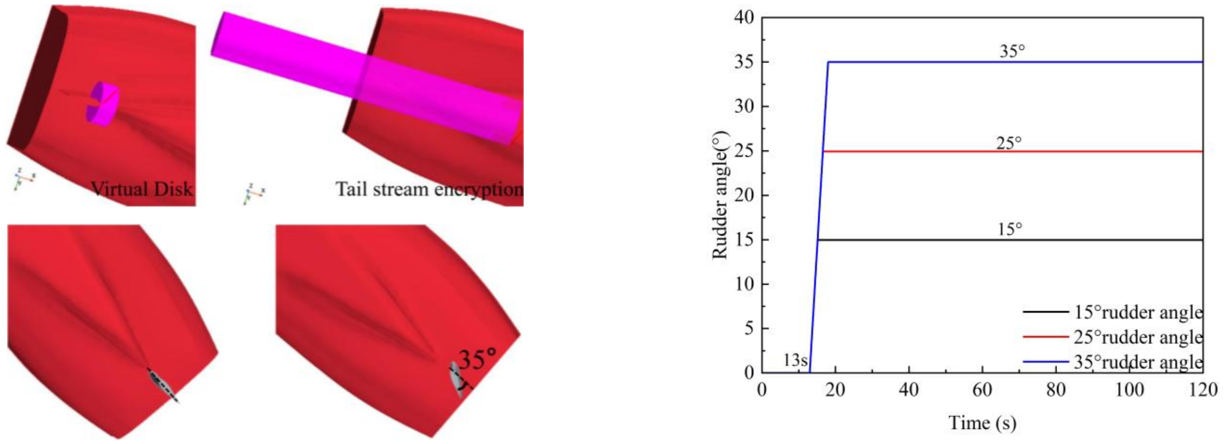

(a) Virtual disk, tail stream encryption, and rudder angle (b) Rudder angle changes with time

Fig. 7 Virtual disk setup, tail stream encryption, rudder angle varies with time

Table 4 Key parameters of the polar ship and the virtual disk model

	Abbreviation	Full- scale	Model-scale	Unit
Longitudinal center gravity	LCG	109.740	3.719	m
Vertical center gravity	VCG	13.013	0.441	m
Virtual disk inner diameter	D_{in}	1.092	0.037	m
Virtual disk outer diameter	D_{out}	7.200	0.244	m
Center of mass coordinates	(3.719, 0.0, 0.441)			m
Total model ship mass	3210.40			kg
Moment of inertia	(613.84, 11501.81, 11501.81)			kg m^2

The rudder is located at the stern of the ship and follows the movement of the ship. The steering mode is to rotate the right rudder from 0° at a constant speed and rotate at an angular speed of 7 °/s. Steering is terminated once the specified rudder angles of 15, 25, or 35° are reached, with 35° being the maximum rudder angle of the model. The steering operation starts at 13 s and stops at different moments depending on the target rudder angle. Figure 7(b) presents a schematic diagram of the time history of the rudder angle.

4.2 Mesh generation and model validation

The computational background domain of the numerical model for the turning maneuver of a polar ship is illustrated in Figure 8. The simulation employed an overset grid technique in conjunction with the virtual disk method, with the rudder deflected at a constant angular velocity of 0.122173 rad/s. In the CFD simulations, the k-ε turbulence model was adopted, while the Volume of Fluid (VOF) method was used to capture the free surface. The inlet, side, top, and bottom boundaries were specified as velocity inlets, whereas the outlet was defined as a pressure outlet. In ship maneuverability research, a time step of 0.02 s is used to simulate the turning performance of polar ships.

To ensure mesh independence, simulations were performed using grids with different levels of refinement. The total thickness and number of prism layers were set to 0.025 m and six layers, respectively. The baseline grid size was scaled in the ratio of 1.414, thereby generating three sets of coarse, medium, and fine grids for evaluating the turning trajectory of the polar ship. The total number of grid cells was approximately 1.915 million, 4.550 million, and 12.232 million. Figure 9 illustrates the turning maneuvering trajectories of the polar ship in open water under different grid densities. By comparing the numerical simulation results obtained from the three mesh configurations, the validation procedure effectively calibrates the ship's steering process, the trajectory of its turning maneuver, and the accuracy of its deceleration behavior. The discrepancies between the numerical and theoretical models remain within an acceptable range.

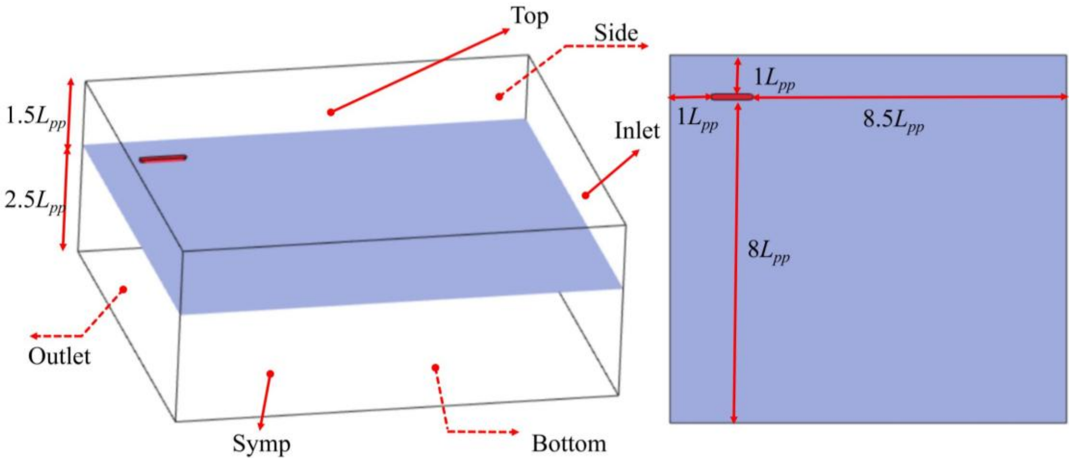

Fig. 8 Numerical computational domain of the polar ship

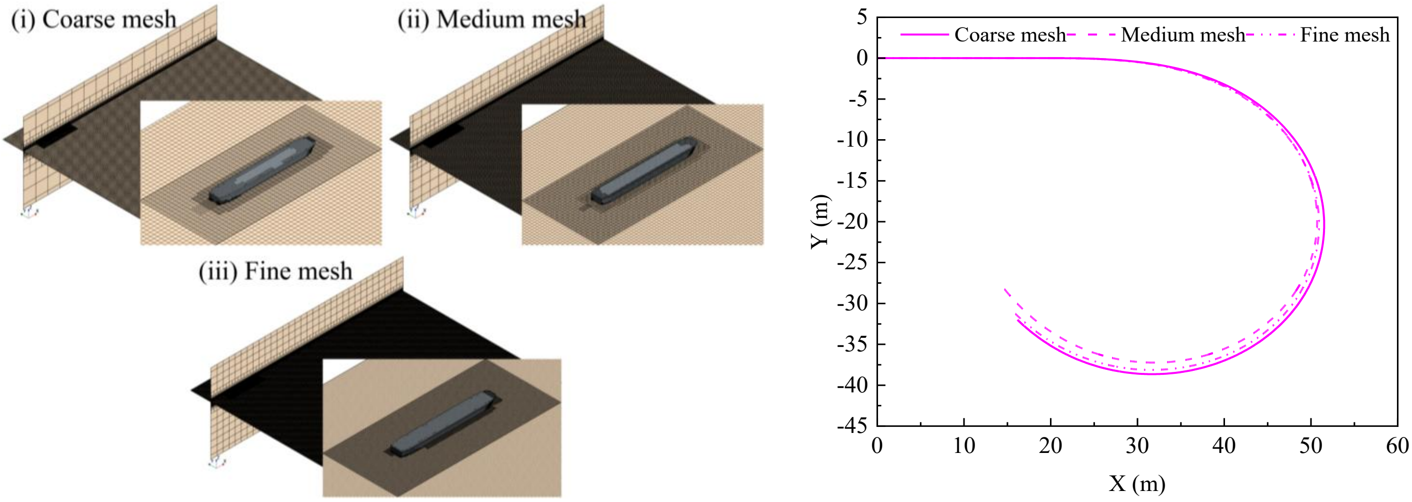

(a) Computational domain meshing (b) Ship turning maneuvering trajectories

Fig. 9 Comparison of turning trajectories under three mesh densities

Numerical simulations revealed that the turning diameters of the polar ship under coarse, medium, and fine mesh densities were 38.651, 37.239, and 38.126 m, respectively. The maximum difference was within 3.8 %. To achieve a more refined representation of the hull and free-surface flow field, while balancing computational efficiency and accuracy, the medium-scale mesh with 4.550 million grids was selected for numerical calculations. In open water, under the medium-scale mesh, the steady resultant speed of the polar ship after stabilization was 0.841 m/s.

5. Results of ship turning ability numerical simulation

5.1 Influence of brash ice geometry

In the field of polar shipping and ocean engineering, the maneuverability of ships operating in ice-covered water is directly related to both navigational safety and operational efficiency. The morphology of brash ice in polar regions varies considerably, and its geometric characteristics—such as ice floe size, outline shape, edge sharpness, and spatial distribution—serve as sensitive parameters influencing a ship's hydrodynamic performance and the ice loads distribution. To further understand the influence of brash ice shape parameters on ship turning trajectories and ice resistance, this section generates brash ice region with different geometric configurations. A series of parameterized brash ice models with distinct shapes, including square, triangular, and circular ice floes, were developed using DEM. The present numerical simulations were conducted based on a one-way coupled CFD–DEM framework. In CFD numerical simulations, the particle surface injector method is employed to generate an idealized brash ice region with uniform concentration.

Comparative analyses were then conducted for three typical ice floe geometries: square, triangular, and circular. The brash ice concentration is maintained at 10 %, with the ice thickness and the top surface area of each ice particle held constant at 0.02 m and 0.042 m², respectively. The dimensions of the different geometric ice floes are illustrated in Figure 10.

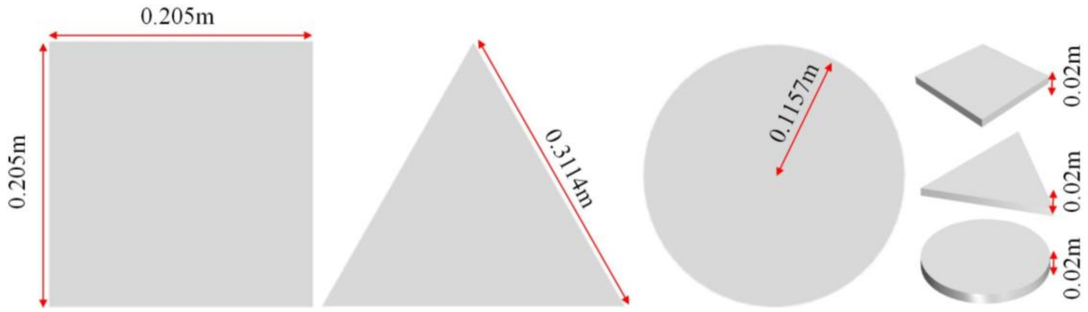

Fig. 10 Ice floe dimensions with three geometric shapes

In all subsequent ice condition studies, the initial ship speed was 1.22 m/s, and the body force model parameters (including the virtual disk rotational speed and imposed force magnitude) were maintained consistent with the open water validation case, with no adjustments made for changes in brash ice conditions. Figure 11 compares the effects of three distinct brash ice geometries on ice resistance in the x direction and the turning maneuvering trajectories of the polar ship, thereby quantifying the underlying mechanisms by which ice geometry influences contact area and collision angle.

From the perspective of longitudinal ice load distribution, the ice load generally attains its initial peak near the bow and subsequently decreases along the ship length. During the early stage of the turning maneuver, the bow first comes into contact with the undisturbed brash ice, generating impact-type loads. As the turning angle increases, brash ice particles accumulate along the outer side of the hull, leading to a gradual shift of the peak load toward the midship region and exhibiting a more sustained blocking effect. In the stern region, the ice load is primarily influenced by the propeller-induced wake and the turning motion of the vessel, resulting in intermittent contact behavior. The overall magnitude of the ice load in this region is lower than that observed in the forward region of the hull. The trend in ice resistance magnitudes can be summarized as follows: Triangular brash ice region > Square brash ice region > Circular brash ice region. This is primarily attributed to the sharp edges of triangular and square ice floes, which induce localized stress concentration during ship–ice interactions, thereby generating larger ice loads on the hull. In contrast, circular ice floes possess continuously curved boundaries without sharp corners, and their nearly uniform equivalent radius distribution results in reduced ship-ice contact forces. The mean heave amplitudes are 0.00255, 0.00265, and 0.00360 m for circular, square, and triangular ice regions, respectively. Furthermore, the heave response amplitude of the ship is largest in triangular ice region, exhibits a moderate level at intermediate frequencies in square ice region, and becomes minimal and more stable in circular ice region.

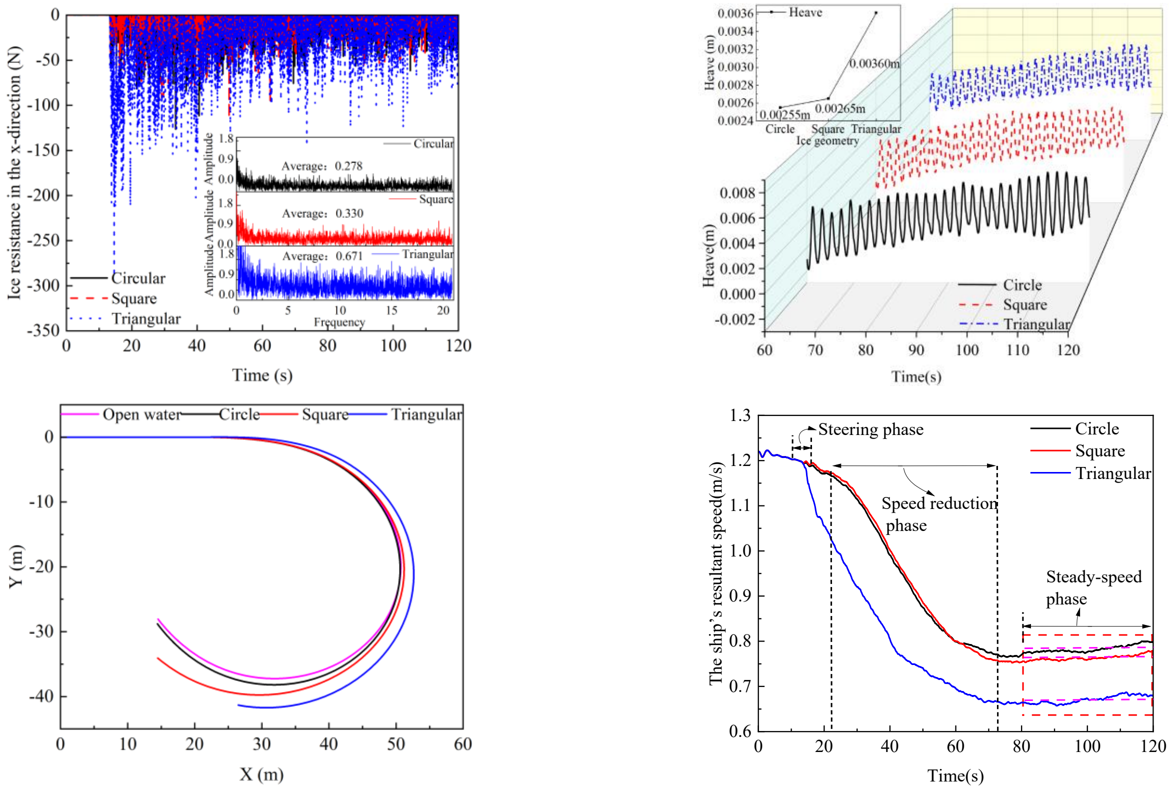

Fig. 11 Ice resistance and turning trajectories time history curves under three ice geometries

Circular brash ice exhibits lower surface roughness, which promotes rolling friction at contact points. Consequently, circular ice regions exert comparatively minor influence on the turning behavior of polar ships, yielding improved maneuverability and higher flexibility. These combined effects account for the superior turning performance observed in circular ice environments. When ice concentration, ice thickness, and floe surface area are kept constant, the tactical diameters of turning trajectories in open water, circular, square, and triangular brash ice regions are 37.239, 38.191, 39.760, and 41.722 m, respectively. Compared with open-water conditions, in the circular brash-ice region with low concentration, the longitudinal advance and tactical diameter exhibit relatively minor variations, whereas in the square and triangular brash-ice regions, both the advance and tactical diameter increase significantly. The turning trajectory length within a fixed time interval is reduced, indicating a deterioration in the ship's turning ability. The results indicate that square and triangular floes with pronounced edges increase the tactical diameter by 6.77 and 12.04 %, respectively, when compared to circular floes. Moreover, within the same computational time, polar ships navigating in square and triangular ice regions exhibit shorter trajectory lengths but larger tactical diameters, reflecting degraded maneuverability. This is primarily attributed to higher ice loads acting on ships in angular floe environments, which reduce trajectory distance while simultaneously compromising turning performance.

Based on the data presented in Figure 11, it is observed that the geometry of brash ice exerts a pronounced influence on the deceleration characteristics of polar ships. Specifically, the steady-state speed of the ship was measured as 0.785 m/s in circular brash ice region, 0.765 m/s in square brash ice region, and 0.672 m/s in triangular brash ice region, respectively. Due to the additional resistance induced by brash ice, the steady-state speed of the polar ship is significantly lower than that in open water. Figure 12 presents the time required for the polar ship to reach different heading angles during turning maneuvers in the square brash ice region, as well as the flow field distribution after the brash ice at the stern is displaced during the ship's navigation.

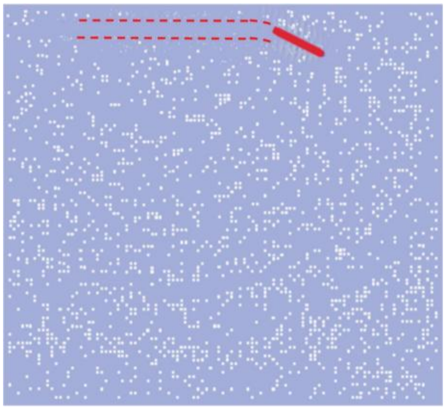

(a) Heading angle is 27° (time=31 s)

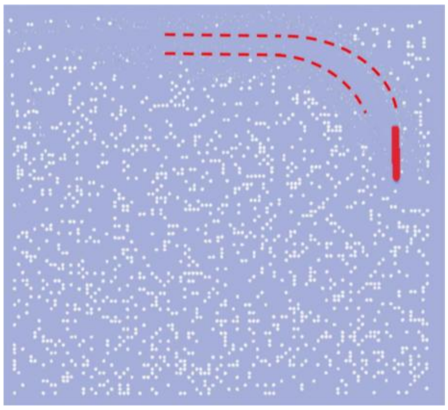

(b) Heading angle is 90° (time=52 s)

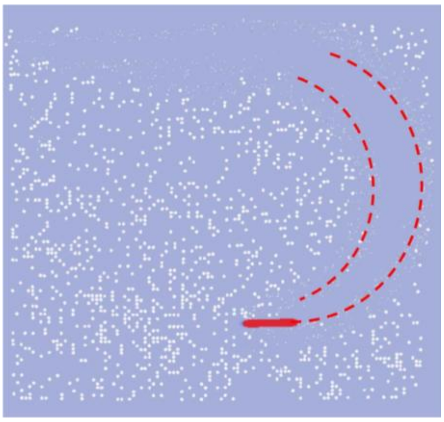

(c) Heading angle is 180° (time=95 s)

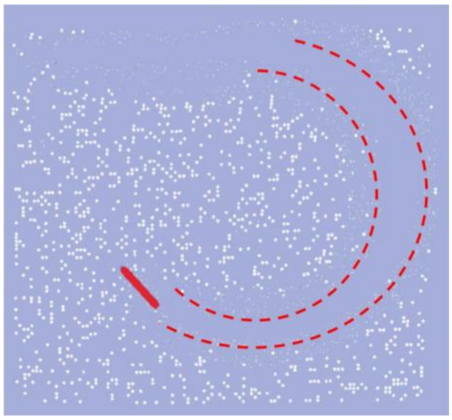

(d) Heading angle is 225° (time=120 s)

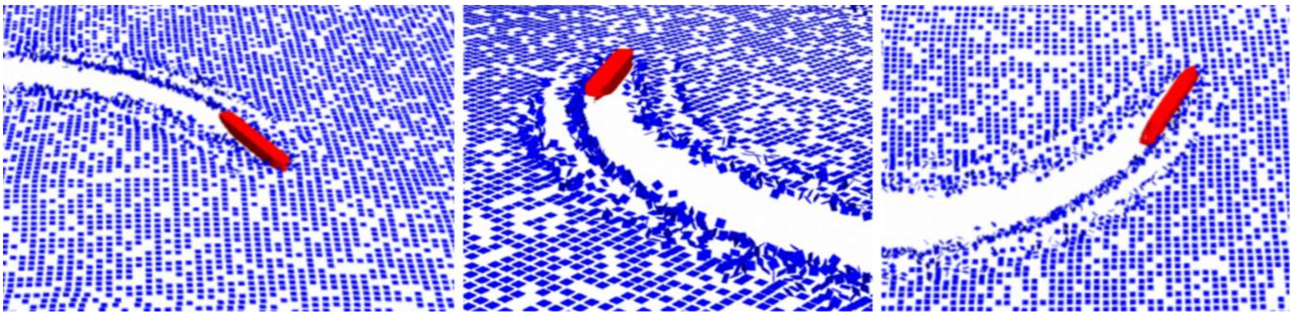

(e) Visualization cloud maps of ship–ice collisions from different perspectives (bow, stern, and hull bottom)

Fig. 12 Ship's heading angles at different times and brash ice distribution on free surface

Analysis of the surface flow field indicates that the polar ship initially maintains a stable straight-line navigation state, during which sea ice predominantly interacts with the bow and shoulder regions of the hull. From the initiation of the starboard rudder maneuver until the ship's heading angle reaches 90°, the dominant ice-ship interaction zones shift, with the inner side of the turning circle, the bow, and the starboard side of the hull becoming the principal load-bearing regions. Figure 13 presents the transverse ice forces under different brash ice geometries, as well as the pressure distribution on the hull-rudder surface at the moment when the ship's turning motion stops. During the turning maneuver of a polar ship, the open water zone aft of the vessel becomes significantly larger than that in straight-line navigation, thereby facilitating the development of a wider navigable channel. In brash ice conditions, the stern shoulder plays an active role in icebreaking by effectively deflecting and displacing the surrounding ice. This interaction leads to the clearance of ice in the stern region and the subsequent formation of an expanded open-water area. In the shoulder and outer midship transitional region, the turning motion introduces a transverse velocity component. Under the combined effects of inertia and the local flow field, brash ice accumulates along the outer side of the hull, forming a longitudinal accumulation band. The pressure distribution reveals a high-pressure zone extending from the shoulder to the outer midship region, which constitutes the primary contributor to the transverse ice force and directly affects turning radius.

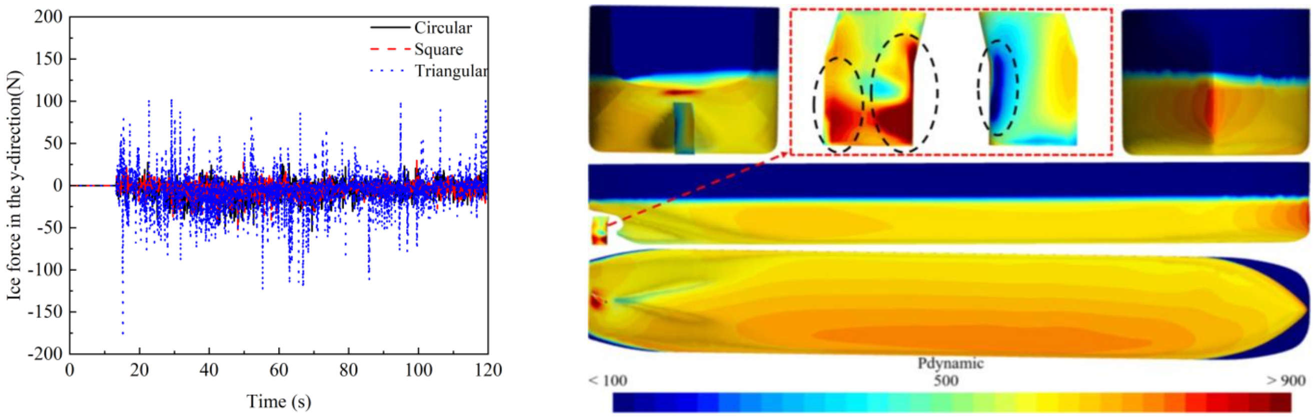

Fig. 13 Ice force in the y direction and hull-rudder surface pressure distribution

The ice force is primarily concentrated in the transition region from the bow to the midship along the outer side of the hull. After the rudder angle is applied, the vessel develops a lateral velocity component, and the outer side of the hull directly encounters the brash ice region. Under the combined effects of inertia and the surrounding flow field, ice floes accumulate along the outer side of the hull, forming a compacted ice band. In this region, frequent contacts among ice particles lead to elevated contact forces per unit area and peak transverse ice force. In contrast, on the inner side of the hull, brash ice floes are gradually displaced away from the ship, resulting in significantly reduced contact intensity and comparatively lower ice loads. At a rudder angle of 35° to starboard, the starboard rudder surface experiences the maximum pressure, while a low-pressure region develops on the port side, generating a rudder moment that sustains the ship's turn. The pressure distribution is characterized by higher values at the leading edge and lower values at the trailing edge. On the port rudder surface, pressure remains low, whereas a stronger concentration appears in the upper starboard region. During the maneuver, the bow experiences increased pressure due to interactions with brash ice and the flow. At the final stage of turning, contact between the portside hull bottom and accumulated brash ice leads to significantly higher surface pressure on the port side compared with the starboard side.

5.2 Influence of the Young's modulus

Currently, most scholars focus on simulating the interaction between marine structures and sea ice, with particular emphasis on predicting the ice loads induced by collisions. However, limited attention has been conducted to examine how micro-scale parameters of sea ice influence the ice loads acting on polar ships, turning trajectories, deceleration characteristics, and multiple degrees of freedom motions. The mechanical properties of sea ice are strongly governed by its Young's modulus. During the elastic deformation regime of a material, the ratio of stress (σ) to strain (ε) is defined as the elastic modulus E, i.e., $E = \sigma / \varepsilon$. E decreases linearly with the brine volume (vb), expressed as $E = 10 - 0.0351 \cdot v_b$ Gpa [42]. In the DEM framework, the adopted Young's modulus mainly serves to characterize the mechanical properties and collision response of sea ice, and its essence is that of an equivalent contact parameter.

Based on a comprehensive review of the literature, the Young's modulus of natural sea ice ranges from 0.3 to 10.4 GPa. To establish the mechanical properties of sea ice for DEM simulations and to investigate their influence on ship maneuvering trajectories, representative Young's modulus values of 1, 4, and 6 GPa were selected. Applying similitude laws for physical scaling, the corresponding model-scale Young's modulus values were determined as 33.889, 133.556, and 203.335 MPa. The brash ice thickness, circular brash ice diameter, ice concentration, and rudder angle were set to 0.02 m, 0.2314 m, 10 %, and 35°, respectively. Poisson's ratio of brash ice is set to 0.3. Given that the rigid body DEM assumption has a limited impact on macroscopic resistance, this assumption is suitable for studies on ship maneuverability in low-speed, brash ice conditions.

These parameters enabled the establishment of quantitative relationships between the microscopic properties of sea ice particles and ship-ice loads, as well as ship maneuvering responses. The resulting ice loads, turning trajectories, and deceleration behaviors of the ship under different sea ice Young's modulus conditions are illustrated in Figure 14.

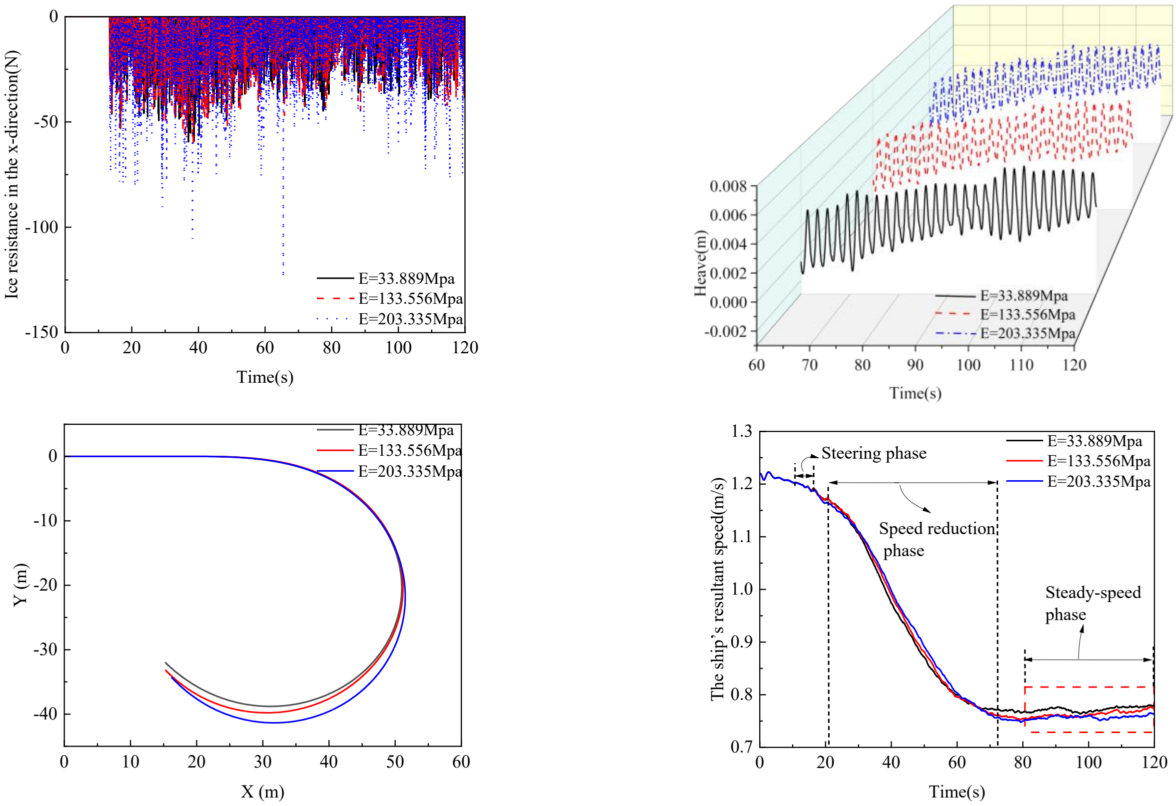

Fig. 14 Ice resistance and motion time history curves of ships under different Young's modulus

Based on the discrete element model and the numerical results of turning ability, it is demonstrated that when the Young's modulus increases from 33.889 to 203.335 MPa, the ice resistance exhibits a pronounced growth trend. This variation in the Young's modulus modifies the stiffness characteristics of brash ice, thereby influencing the magnitude of ice loads, amplitude fluctuations, duration, and spatial distribution during ship-ice collisions. Consequently, these changes affect the stability of ship turning motions and propulsion efficiency, exerting a series of impacts on the ice resistance performance, turning maneuvering, propulsion performance, speed reduction, and heave response of polar ships.

On the turning ability of polar ships, the presence of brash ice with a high Young's modulus results in greater ice resistance, thereby diminishing the ship's turning performance. Numerical simulations indicate that an increase in the Young's modulus of brash ice leads to a marked reduction in rudder effectiveness. Specifically, when the Young's modulus of brash ice is 33.889, 133.556, and 203.335 MPa, the corresponding turning diameters of the ship are 38.801, 39.793, and 41.356 m, respectively. Compared with the low Young's modulus case (E=33.889 Mpa), the turning diameter increases by 2.56 and 6.58 % under medium and high Young's modulus conditions.

Under identical initial speeds and engine power, the stabilized mean speeds of the polar ship navigating in brash ice region with high Young's modulus (E=203.335 MPa), medium Young's modulus (E=133.556 MPa), and low elastic modulus (E=33.889 MPa) were 0.757, 0.768, and 0.774 m/s, respectively. Compared with the low young's brash ice condition (E=33.889 MPa), the speed losses in the high modulus and medium modulus brash ice regions were approximately 2.20 and 0.78 %, respectively. Moreover, the reduction in ship speed exhibited a pronounced nonlinear characteristic. Figure 15. presents the energy contour map of ice particles generated during ship-ice collisions in the turning maneuver, with the ice Young's modulus set to 133.556 MPa.

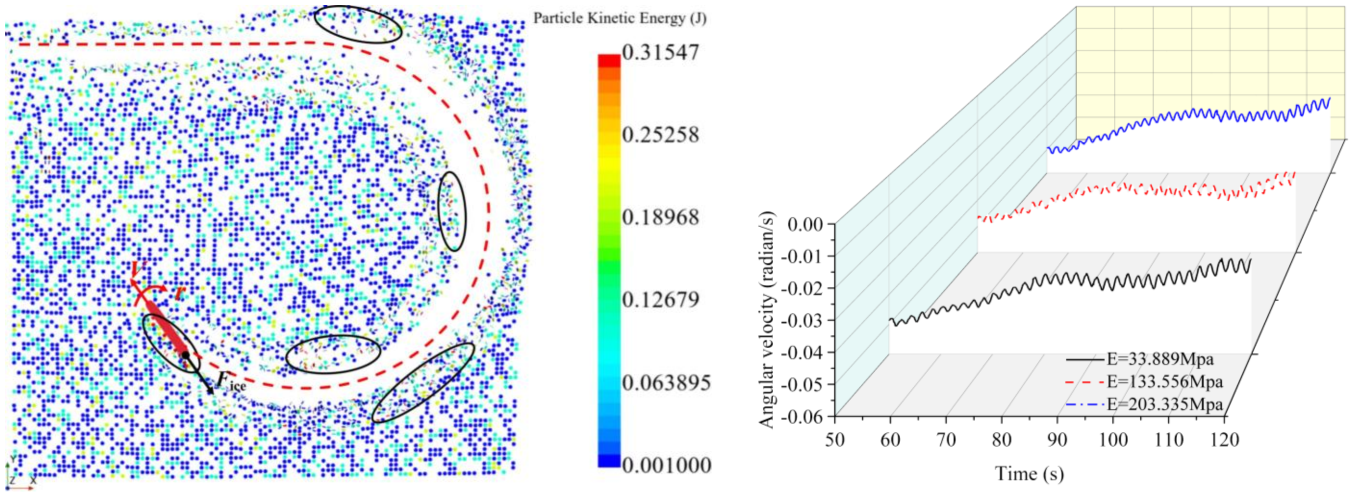

Fig. 15 Energy contour map of ice particles and time-history curve of turning angular velocity

During the turning maneuver of a polar ship, the energy cloud of brash ice particles exhibits a distinct pattern of localized concentration. Significant particle energy accumulation is observed at the bow and midship regions due to frequent ship-ice collisions. Along both sides of the ship's trajectory, the combined effects of wave-making and collisions lead to increased particle energy, accompanied by phenomena such as the overturning of brash ice particles. In the bow region, the kinetic energy of ice particles is significantly converted into contact dissipation energy, indicating that this area represents the primary energy dissipation zone of the ice–hull interaction. Therefore, the collision and accumulation of brash ice at the bow determine the occurrence of the resistance peak during the early stage of turning.

Numerical results indicate that when the ship's heading angle reaches 90°, the turning angular velocity of the polar ship increases noticeably under different ice Young's modulus conditions. Owing to the intensified energy dissipation during the turning maneuver, the overall angular velocity remains relatively low. When the turning process reaches approximately 80 s, the angular velocity tends to stabilize, exhibiting only minor fluctuations. Collisions with high Young's modulus ice are more likely to generate abrupt, high-amplitude impact forces, which suppress the continuous turning motion of the ship and induce additional fluctuations and reductions in angular velocity.

5.3 Influence of rudder angle

In this section, the unresolved issue of the coupled ship-ice-water multiphysics interaction mechanism during turning maneuvers in brash ice regions is addressed. Trajectory predictions of a polar ship under various rudder operations in brash ice regions with an ice concentration of 40 % are carried out. Our research group has previously performed numerical validation against the HSVA ice tank tests conducted in a real brash ice channel, where the target brash ice thickness was 1.452 m [32]. According to the ice thickness similarity law, the corresponding model ice thickness was determined to be 0.0492 m, with a representative square brash ice floe size of 0.4 m. The initial forward speed of the polar ship was set to 1.22 m/s. Figure 16 presents the time histories of ice resistance, heave motion, turning trajectories, and speed reduction.

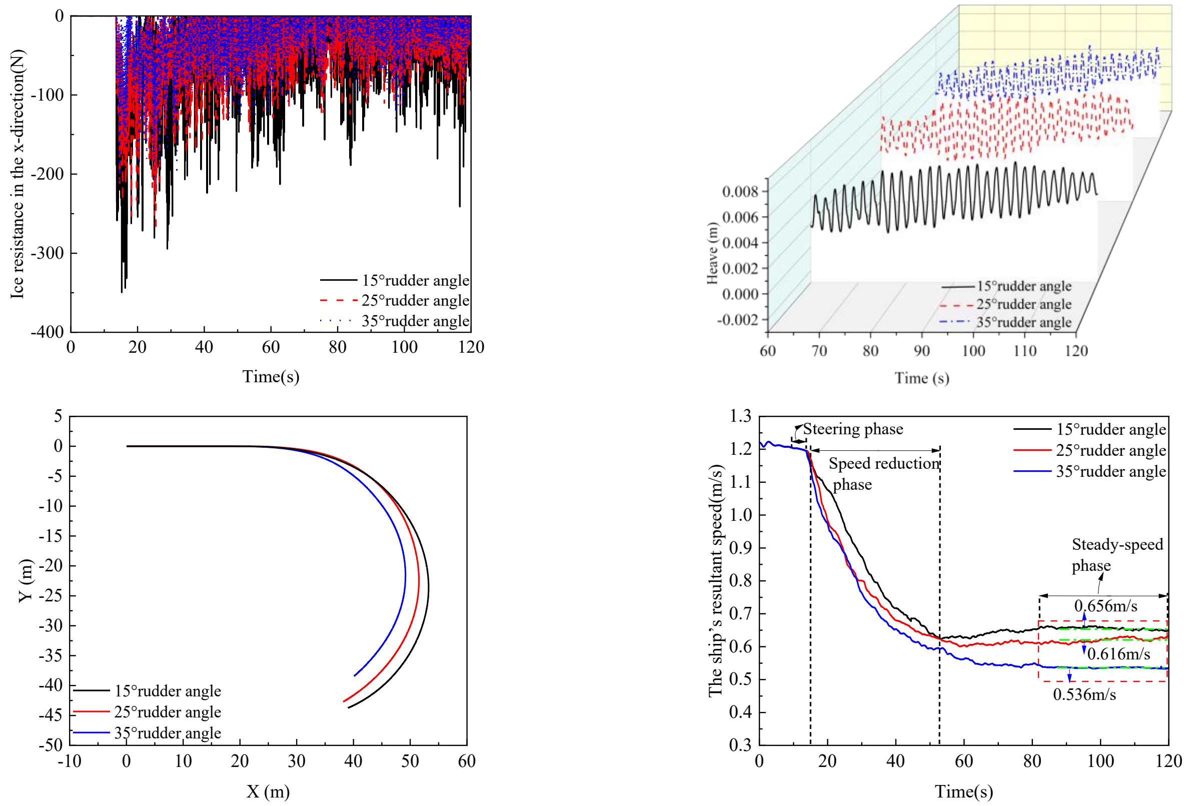

Fig. 16 Comparison of ship turning trajectories and speed reduction at different rudder angles

By constructing a representative mesh and adjusting the injector flow rate, a total of 7,540 DEM brash ice particles were rapidly released onto the water surface. The results indicate that when the polar ship performs turning maneuvers with relatively small rudder angles, the deceleration effect is weaker. Consequently, the ship maintains a higher steady-state speed at small rudder angles, leading to greater kinetic energy during ship-ice collisions. As a result, the longitudinal ice load acting on the polar ship exhibits a larger amplitude.

During the turning motion of the polar ship after colliding with brash ice, a pronounced lifting phenomenon is observed. Due to frequent and intense collisions between the hull and a large number of randomly distributed brash ice, localized, asymmetric, and high-frequency impact loads are generated, which in turn make the ship's motion response more complex. The heave motion is particularly prominent, as direct impacts between the ship's bottom, bow, and the ice fragments induce vertical upward forces. Each collision between the brash ice and the ship generates an impulsive upward force, resulting in a certain degree of jacking or lifting of the ship. Analysis of the heave time-history curve further reveals an overall upward trend.

Influenced by the combined effects of ice-water resistance and rudder action, the mean steady-state speeds of the ship at rudder angles of 15, 25, and 35° are 0.656, 0.616, and 0.536 m/s, respectively. These values are significantly lower than the steady turning speeds in open water. With increasing rudder angle, the turning trajectory within the same computational time is noticeably shortened in brash ice. However, if the simulation time is extended, the tactical diameter, advance, and turning radius all increase compared with open-water conditions, and the stabilized speed of the polar ship remains significantly lower than that in open water. Figure 17(a) presents a comparison of the steady speeds of the polar ship during turning maneuvers in open water and in brash ice conditions.

A representative case with a rudder angle of 35° was selected to investigate the forces acting in three distinct directions, and the corresponding time history curves were subsequently subjected to smoothing processing. Figure 17(b) presents the rudder force curves in different directions at a rudder angle of 35° during the ship's turning maneuver. Figure 17(c) shows the yaw moment of the polar ship under different rudder angles.

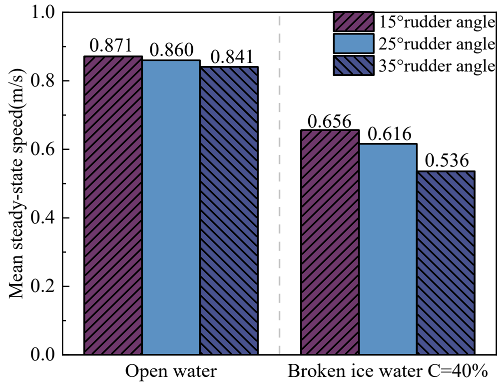

(a) Ship speed in steady state

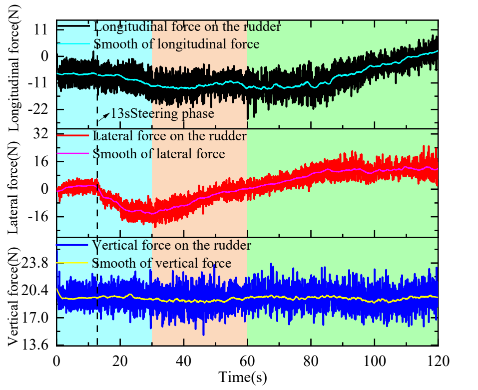

(b) Forces on the rudder in different directions

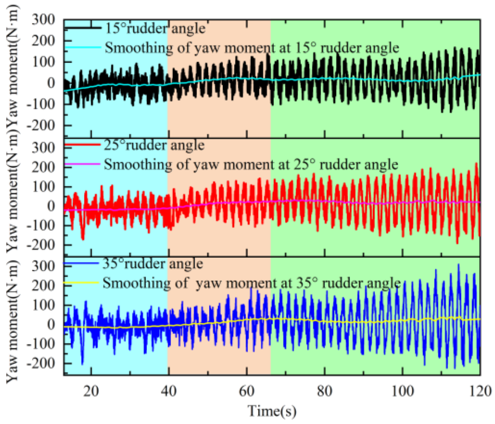

(c) Yaw moment

Fig. 17 Ship's mean steady-state speed, rudder forces and yaw moment

The combined effects of ship steering, turning maneuvers, and ice-water interactions exert a significant influence on both the forces and directional behavior of the rudder. During the initiation of steering at 13 s, the rudder exhibited maximum sensitivity in lateral force. Throughout the turning process, the lateral force on the rudder gradually increases, fluctuates around 16 N, then decreases to 0 N, and subsequently grows in the opposite direction until reaching a stable state. The final mean lateral force on the rudder is 13.54 N, which is significantly smaller than the force in the Z-axis direction. In the rudder region, the force acting on the rudder changes significantly with rudder angle. During steering, the rudder alters the wake direction, resulting in increased velocity asymmetry behind the rudder. This asymmetric wake structure influences the variation of rudder forces. In turn, changes in rudder loading modify the flow distribution, thereby indirectly affecting the development of the ship's turning speed. With the brash ice concentration and floe size kept constant, the yaw moment of the polar ship oscillates around zero throughout the turning maneuver. However, the rudder angle has a significant influence on the yaw moment response. As the rudder angle increases, both the peak values and fluctuation amplitudes of the yaw moment increase markedly. These fluctuations are primarily caused by changes in the ship's speed induced by rudder action and the increased frequency of ship-ice collisions. In addition, the yaw moment response exhibits relatively high frequency oscillations, reflecting the random interaction between the hull and surrounding brash ice floes.

In the numerical simulations of the maneuvering motion of the polar ship, the rotational speed of the virtual disk was maintained at 8.5 r/s, a representative brash ice condition was selected, with the rudder angle set to 35°. The resulting body forces and moments acting on the virtual disk are presented in Figure 18.

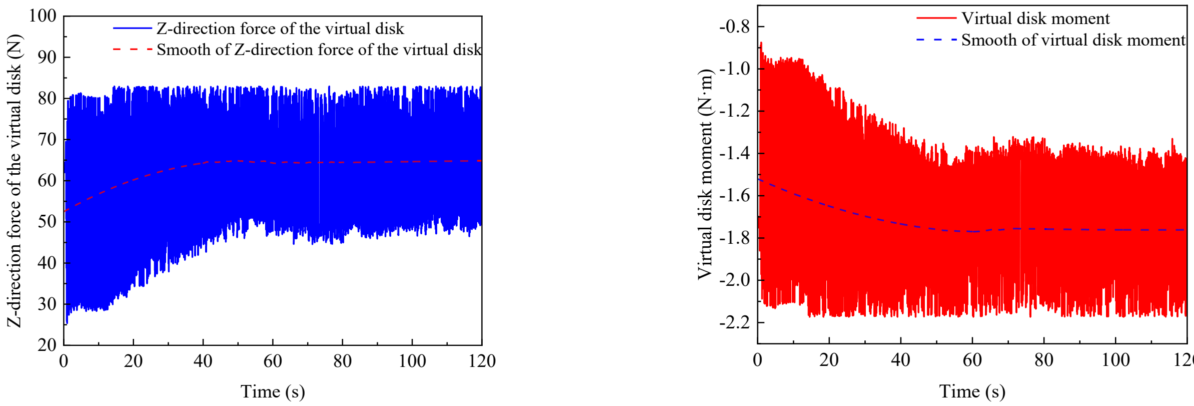

Fig. 18 Virtual disk force and virtual disk moment

It was further observed that, under the same rotational speed of the virtual disk, the variation ranges of both the virtual disk moment and the axial (z-direction) body force remained consistent across different rudder angles. At a rudder angle of 35°, the mean values of the virtual disk body force and body moment were 65.191 N and 1.761 N·m, respectively. In the virtual disk region, the downstream flow exhibits an axial acceleration characteristic. The propeller disk region regulates the moment distribution, and the brash-ice velocity field shows localized acceleration downstream of the disk.

6. Conclusion

This study uses unsteady RANS-based CFD-DEM coupling approach to investigate the factors that influence ice loads, turning trajectories, deceleration behavior, and multi-degree-of-freedom motions of a polar ship. The main conclusions are summarized as follows:

(1) A numerical model of a brash ice channel was developed using the DFBI plane motion mechanism to simulate the interaction between a polar ship and surrounding brash ice. The numerical results showed good agreement with experimental data and the FSICR empirical formulation, confirming the reliability of the numerical method.

(2) Based on the overset grid technique and the body force method (BFM), the maneuvering trajectories of a polar ship were simulated under different grid resolutions. The results showed good agreement among the turning trajectories, confirming the reliability of the adopted numerical method for maneuvering simulations.

(3) A systematic analysis based on the discrete element method was conducted to investigate the influence of different ice geometries on ice loads and maneuvering performance. With ice thickness, concentration, and surface area kept constant, the ice resistance exhibited the following trend: triangular ice floes > square ice floes > circular ice floes, mainly due to differences in edge distribution and surface roughness. Higher ice loads in triangular brash ice regions weakened the turning ability of the polar ship, resulting in larger turning diameters and deteriorated maneuverability.

(4) This study investigated the influence of sea ice mechanical properties on ship turning ability and ice resistance. An increase in the Young's modulus of sea ice significantly increases ice resistance and weakens the turning performance of the ship due to the enhanced stiffness of sea ice, resulting in reduced angular velocity, lower ship speed, larger turning diameter, and decreased rudder effectiveness.

(5) A numerical analysis of the turning maneuvers of a polar ship under different rudder angles was conducted. Smaller rudder angles resulted in weaker deceleration, higher steady-state speeds, and larger longitudinal ice loads. Frequent ship-ice collisions significantly enhanced the heave motion of the ship, while the lateral rudder force exhibited an initial increase, followed by a decrease and eventual stabilization in the opposite direction. The yaw moment response is highly sensitive to rudder angle, with larger rudder angles leading to greater fluctuation amplitudes and peak values.

This study also has several unaddressed limitations. The brash ice region is composed of uniform, non-breakable small ice fragments with low to medium concentration. Factors such as ice ridges, icebergs, level ice, and their stochastic combinations in polar environments were not considered. The superimposed effects of environmental forces such as wind and waves on brash ice and ship maneuverability were also neglected. In the future, the influence of the above factors on polar ship maneuverability will be considered. The BFM method adopted in this paper is a body force model based on instantaneous flow field updates, rather than a fully steady-state assumption. It does not consider direct ice–propeller contact, and the propulsion process is an engineering simplification. Furthermore, the BFM has certain limitations under high-concentration brash ice conditions.

ACKNOWLEDGMENTS

This work was supported by Shanghai Merchant Ship Design & Research Institute (SDARI) in China "Research on optimized polar environmental protection transport ships", Natural Science Foundation of Liaoning Province (2024-MS-016); China COSCO Shipping Corporation Limited (Numerical and Experimental Technology Research of Ship Navigation Performance in the High Sea States, 2023-2-Z001-02-01); Dalian City's Public Recruitment Project for Key Technical Challenges (Grant No. 2023JB11SN006) and the Fundamental Research Funds for the Central Universities of China (3132025617).

REFERENCES

[1] Huang, L. F., Tuhkuri, J., Igrec, B., Li, M., Stagonas, D., Toffoli, A., et al., 2020. Ship resistance when operating in floating ice floes: A combined CFD&DEM approach. *Marine Structures*, 74, 102817. https://doi.org/10.1016/j.marstruc.2020.102817

[2] Luo, W., Jiang, D., Wu, T., Guo, C., Wang, C., Deng, R., Dai, S., 2020. Numerical simulation of an ice-strengthened bulk carrier in brash ice channel. *Ocean Engineering*, 196, 106830. https://doi.org/10.1016/j.oceaneng.2019.106830

[3] Xie, C., Zhou, L., Ding, S., Lu, M., Zhou, X., 2023. Research on self-propulsion simulation of a polar ship in a brash ice channel based on body force model. *International Journal of Naval Architecture and Ocean Engineering*, 15, 100557. https://doi.org/10.1016/j.ijnaoe.2023.100557

[4] Zou, M., Zou, Z. J., Zou, L., Chen, C. Z., Zhang, X. S., 2024. Numerical investigations of the ice force distributions on a ship in brash ice channel using a simplified CFD-DEM solving framework. *Ocean Engineering*, 312, 119103. https://doi.org/10.1016/j.oceaneng.2024.119103

[5] Yasukawa, H., Yoshimura, Y., 2015. Introduction of MMG standard method for ship maneuvering predictions. *Journal of Marine Science and Technology*, 20(1), 37-52. https://doi.org/10.1007/s00773-014-0293-y

[6] Kim, H., Im, N., Sawamura, J., 2017. Experimental and Numerical Investigation of Ship–Ice Interactions in Pack Ice. *Proceedings of the 24th International Conference on Port and Ocean Engineering under Arctic Conditions* (POAC 2017), 11-16 June, Busan, Korea.

[7] Zhou, Q., Peng, H., Qiu, W., 2016. Numerical investigations of ship–ice interaction and maneuvering performance in level ice. *Cold Regions Science and Technology*, 122, 36-49. https://doi.org/10.1016/j.coldregions.2015.10.015

[8] Yang, B., Yang, B., Zhang, G., Zhang, A., Sun, Z., 2025. Numerical Simulation of Ship Star Maneuver in Broken Ice Region Based on NDEM. *Proceedings of the 35th International Ocean and Polar Engineering Conference* (ISOPE-2025), 1-6 June, Seoul, Korea, Paper No. ISOPE-I-25-323.

[9] Wang, D., Zou, L., Zhang, Z., Chen, X., 2025. Numerical Study on Non-Icebreaking Ship Maneuvering in Floating Ice Based on Coupled NDEM–MMG Modeling. *Journal of Marine Science and Engineering*, 13, 1578. https://doi.org/10.3390/jmse13081578

[10] Lau, M., 2006. Discrete element modeling of ship manoeuvring in ice. *18th IAHR International Symposium on Ice*, 28 August – 1 September, Sapporo, Japan.

[11] Zhan, D., Agar, D., He, M., Spencer, D., Molyneux, D., 2010. Numerical simulation of ship maneuvering in pack ice. International *Conference on Offshore Mechanics and Arctic Engineering* (OMAE 2010), 6-11 June, Shanghai, China. https://doi.org/10.1115/OMAE2010-21109

[12] Huang, L. F, Li, F., Li, M. H, Khojasteh, D., Luo, Z. H, Kujala, P., 2022. An investigation on the speed dependence of ice resistance using an advanced CFD+ DEM approach based on pre-sawn ice tests. *Ocean Engineering*, 264, 112530. https://doi.org/10.1016/j.oceaneng.2022.112530

[13] Zhang, J. L., Zhang, J. N., Zhang, L., Chen, W. M., Zhang, Q. S., 2025. Numerical Research on Hull–Propeller–Rudder–Ice Interaction of Full-Scale Polar Transport Ship in Brash Ice Channel. *Journal of Marine Science and Engineering*, 13(1), 145. https://doi.org/10.3390/jmse13010145

[14] Zhong, K., Ni, B. Y., Li, Z. Y., Xu, X. S., Wei, H. Y., Li, H. Y., Xue, Y. Z., 2023. Direct measurements and CFD simulations on ice-induced hull pressure of a ship in floe ice fields. *Ocean Engineering*, 272, 113523. https://doi.org/10.1016/j.oceaneng.2022.113523

[15] Ni, B. Y., Chen, Z. W., Zhong, K., Li, X. A., Xue, Y. Z., 2020. Numerical simulation of a polar ship moving in level ice based on a one-way coupling method. *Journal of Marine Science and Engineering*, 8(9), 692. https://doi.org/10.3390/jmse8090692

[16] Li, L., Han, G. C., Ji, S. Y., 2024. Statistical analysis of ice load on icebreaker ship based on stochastic ice fields. *Journal of Marine Science and Engineering*, 12(3), 448. https://doi.org/10.3390/jmse12030448

[17] Zhang, J., Gaidai, O., Wang, K. M., Xu, J. H., Ye, R. C., Xu, X. S., 2019. A stochastic method for the prediction of icebreaker bow extreme stresses. *Applied Ocean Research*, 87, 95-101. https://doi.org/10.1016/j.apor.2019.03.019

[18] Wang, C., Hu, X. H., Tian, T. P., Guo, C. Y., Wang, C. H., 2020. Numerical simulation of ice loads on a ship in broken ice fields using an elastic ice model. *International Journal of Naval Architecture and Ocean Engineering*, 12, 414-427. https://doi.org/10.1016/j.ijnaoe.2020.03.001

[19] Jeon, S., Kim, Y., 2022. Fatigue damage estimation of icebreaker ARAON colliding with level ice. *Ocean Engineering*, 257, 111707. https://doi.org/10.1016/j.oceaneng.2022.111707

[20] Liu, R. W., Xue, Y. Z., Lu, X. K., 2023. Coupling of Finite Element Method and Peridynamics to Simulate Ship-Ice Interaction. *Journal of Marine Science and Engineering*, 11(3), 481. https://doi.org/10.3390/jmse11030481

[21] Chen, Z., He, Y. P., Gu, Y. B., Su, B., Ren, Y. P., Liu, Y. D., 2021. A novel method for numerical simulation of the interaction between level ice and marine structures. *Journal of Marine Science and Technology*, 26(4), 1170-1183. https://doi.org/10.1007/s00773-021-00799-w

[22] Chen, Z., He, Y. P., Ren, Y., Ren, Y. P., Liu, Y. D., 2022. Numerical simulation on an icebreaking vessel with fixed drift angles in level ice. *Ocean Engineering*, 244, 110382. https://doi.org/10.1016/j.oceaneng.2021.110382

[23] Xu, P., Chen, B. L., Guo, Y. C., Wang, H., 2024. Numerical Simulation Study on Ice–Water–Ship Interaction Based on FEM-SPH Adaptive Coupling Algorithm. *Water*, 16(22), 3249. https://doi.org/10.3390/w16223249

[24] Zhang, N. B., Zheng, X., Ma, Q. W., 2017. Updated smoothed particle hydrodynamics for simulating bending and compression failure progress of ice. *Water*, 9(11), 882. https://doi.org/10.3390/w9110882

[25] Zhang, N. B., Zheng, X., Ma, Q. W., Hu, Z. H, 2019. A numerical study on ice failure process and ice-ship interactions by Smoothed Particle Hydrodynamics. *International Journal of Naval Architecture and Ocean Engineering*, 11(2), 796-808. https://doi.org/10.1016/j.ijnaoe.2019.02.008

[26] Su, B., Riska, K., Moan, T., 2010. A numerical method for the prediction of ship performance in level ice. *Cold Regions Science and Technology*, 60(3), 177-188. https://doi.org/10.1016/j.coldregions.2009.11.006

[27] Su, B., Riska, K., Moan, T., 2011. Numerical study of ice-induced loads on ship hulls. *Marine Structures*, 24(2), 132-152. https://doi.org/10.1016/j.marstruc.2011.02.008

[28] Su, B., Skjetne, R., Berg, T. E., 2014. Numerical assessment of a double-acting offshore vessel's performance in level ice with experimental comparison. *Cold Regions Science and Technology*, 106, 96-109. https://doi.org/10.1016/j.coldregions.2014.06.012

[29] Zhou, Q., Heather, P., Qiu, W., 2016. Numerical investigations of ship–ice interaction and maneuvering performance in level ice. *Cold Regions Science and Technology*, 122, 36-49. https://doi.org/10.1016/j.coldregions.2015.10.015

[30] Gu, Y. J., Zhou, L., Ding, S. F., Tan, X., Gao, J. L., Zhang, M., 2022. Numerical simulation of ship maneuverability in level ice considering ice crushing failure. *Ocean Engineering*, 251, 111110. https://doi.org/10.1016/j.oceaneng.2022.111110

[31] Xuan, S. Y., Zhan, C. S., Liu, Z. Y., Zhao, Q. S., 2021. Numerical research on global ice loads of maneuvering captive motion in level ice. *Journal of Marine Science and Engineering*, 9(12), 1404. https://doi.org/10.3390/jmse9121404

[32] Xuan, S. Y., Zhan, C. S., Liu, Z. Y., Feng, B. W., Chang, H. C., Wei, X., 2023. Numerical Investigation of Global Ice Loads of Maneuvering Captive Motion in Ice Floe Fields. *Journal of Marine Science and Engineering*, 11(9), 1778. https://doi.org/10.3390/jmse11091778

[33] Yang, B. R., Zhang, G. Y., Rao, H. H., Wang, S. S., Yang, B. Y., Sun, Z., 2024. Numerical simulation of the maneuvering performance of ships in broken ice area. *Ocean Engineering*, 294, 116783. https://doi.org/10.1016/j.oceaneng.2024.116783

[34] Zhang, J. L., Zhang, J. N., Zhang, L., Qi, K. F., Wang, H. Y., 2025. Research on ice resistance and maneuvering performance of ships in broken ice region. *8th International Conference on Material Strength and Applied Mechanics* (MSAM 2025), 10-13 July, Shenzhen, China. https://doi.org/10.1049/icp.2025.2650

[35] Cundall, P. A., Strack, O. D. L., 1979. Discussion: A discrete numerical model for granular assemblies. *Geotechnique*, 30(3), 331-336. https://doi.org/10.1680/geot.1980.30.3.331

[36] Zhang, J. N., Zhang, Y., Shang, Y. C., Jin, Q., Zhang, L., 2022. CFD-DEM based full-scale ship-ice interaction research under FSICR ice condition in restricted brash ice channel. *Cold Regions Science and Technology*, 194, 103454. https://doi.org/10.1016/j.coldregions.2021.103454

[37] HSVA, 2022. Brash Ice Tests for 68k MPV with Ice Class 1A, Appendix A Photos.

[38] Chen, J. M., Chen, Z., Wang, D., Zhang, Y., He, Y., 2024. Prediction and empirical formula correction for brash ice resistance using CFD-DEM based on invisible bulbous bow ship. *Ocean Engineering*, 310, 118752. https://doi.org/10.1016/j.oceaneng.2024.118752

[39] Zheng, S. J., Song, B. Y., Zhou, L., Huang, Q. G., Xie, C., Li, H., et al., 2025. Research on the ice resistance and propulsion performance of polar ships via the CFD-DEM coupling method. *China Ocean Engineering*, 39(2), 232-243. https://doi.org/10.1007/s13344-025-0024-7

[40] Sun, H. S., Ni, X., Zhang, Y. X., Chen, K., Ni B.Y., 2023. A Numerical Prediction of the Resistance of Bulk Carriers in Brash Ice Channels. *Journal of Marine Science and Engineering*, 11(7), 1425. https://doi.org/10.3390/jmse11071425

[41] Xue, Y. Z., Zhong, K., Ni, B. Y., Li, Z. Y., Bergström, et al., 2024. A combined experimental and numerical approach to predict ship resistance and power demand in broken ice. *Ocean Engineering*, 292, 116476. https://doi.org/10.1016/j.oceaneng.2023.116476

[42] Garry, W. T., Wilford, F. W., 2010. A review of the engineering properties of sea ice. *Cold Regions Science and Technology*, 60(2), 107-129. https://doi.org/10.1016/j.coldregions.2009.10.003